From diffraction to imaging: New avenues in studying hierarchical biological tissues with x-ray microbeams (Review)

Oskar Paris[a)]

Department of Biomaterials, Max-Planck Institute of Colloids and Interfaces, Research Campus Golm, 14424 Potsdam, Germany

Load bearing biological materials such as bone or arthropod cuticle have optimized mechanical properties which are due to their hierarchical structure ranging from the atomic/molecular level up to macroscopic length scales. Structural investigations of such materials require new experimental techniques with position resolution ideally covering several length scales. Beside light and electron microscopy, synchrotron radiation based x-ray imaging techniques offer excellent possibilities in this respect, ranging from full field imaging with absorption or phase contrast to x-ray microbeam scanning techniques. A particularly useful approach for the study of biological tissues is the combination x-ray microbeam scanning with nanostructural information obtained from x-ray scattering [small-angle x-ray scattering (SAXS) and wide-angle x-ray scattering (WAXS)]. This combination allows constructing quantitative images of nanostructural parameters with micrometer scanning resolution, and hence, covers two length scales at once. The present article reviews recent scanning microbeam SAXS/WAXS work on bone and some other biological tissues with particular emphasis on the imaging capability of the method. The current status of instrumentation and experimental possibilities is also discussed, and a short outlook about actual and desirable future developments in the field is given. © *2008 American Vacuum Society.* [DOI: 10.1116/1.2955443]

I. INTRODUCTION

From a viewpoint of materials science, biological tissues such as wood, bone, or insect cuticle are composites with a hierarchical structure. Some of them are mineralized, i.e., they form organic/inorganic nanocomposites typically consisting of a fibrous matrix reinforced with crystalline or amorphous nanoparticles. Bone, teeth, and antler, for instance, consist of a fibrous protein matrix (mainly collagen) reinforced with crystalline calcium phosphate nanoparticles.[1–3] On the contrary, wood cell walls usually do not contain any substantial amount of minerals, being polymer/polymer composites of crystalline cellulose nanofibrils in an amorphous matrix of hemicelluloses and lignin.[3–5] Arthropods have an exoskeleton build of a polymer/polymer composite (chitin/protein),[6,7] in some cases—e.g., in crustaceans—additionally reinforced with amorphous and/or crystalline calcium carbonate.[6,8] All these materials show exceptional mechanical properties, which are believed to be due to a functional adaptation of the structure at all levels of hierarchy (see, e.g., Ref. 3). The first step toward a deeper understanding of the structure-function relationships is the detailed characterization of the structure at all hierarchy levels. This can be achieved by applying and combining several position sensitive techniques such as light microscopy, scanning electron microscopy (SEM) and transmission electron microscopy (TEM) combined with elemental analysis, scanning probe microscopy, as well as Raman and infrared spectroscopic imaging. X-ray imaging—in particular, in combination with synchrotron radiation—represents another broad class of useful methods for the investigation of biological tissues. This includes both, full field techniques such as absorption and phase contrast imaging and tomography, as well as x-ray microbeam scanning methods using different sources of contrast. A very powerful recent approach is the application of scanning small-angle x-ray scattering (SAXS) and/or wide-angle x-ray scattering (WAXS) to map local nanostructural features in spatially heterogeneous systems.[9–11] Even though being much slower as compared to full field imaging, one of the big advantages is that the information gained from the nanometer scale is quantitative. Moreover, two spatial regions from different length scales are covered simultaneously, i.e., the nanometer length scale ($\approx 0.1-100$ nm) with the information deduced from x-ray scattering, and the micrometer scale by scanning the specimen across an x-ray beam of some micrometer size.

The rapid increase in the beam brilliance at third generation synchrotron radiation sources in recent years, together with the development of focusing optics for hard x rays has led to the construction of dedicated microfocus beamlines. Pioneering work in the field of microbeam diffraction stems from Riekel *et al.* at the microfocus beamline (ID13) at the European Synchrotron Radiation Facility (ESRF) in Grenoble, France. This group has introduced many cutting-edge developments in instrumentation (see Refs. 11–13 for reviews), and has applied them particularly to polymers and biopolymers.[13–17] User applications at the ID13 beamline include many fields of modern materials science covering among others metals,[18] carbon fibers,[19] synthetic polymers,[20–22] as well as biopolymers and biological tissues.[23–29] In the meanwhile, x-ray microbeams with high photon flux are available also at other sites, and dedicated instruments for

[a)]Electronic mail: oskar.paris@mpikg.mpg.de

scanning SAXS/WAXS have been built[30] or are in the construction phase. Particularly important for the success of microbeam SAXS/WAXS techniques is also the recent development of high resolution area detectors for x-ray scattering. This permits the combination of SAXS and WAXS with one single area detector, providing simultaneous information about the crystal structure and crystallographic texture (WAXS) as well as size, shape, and orientation of nanoparticles or nanofibers (SAXS) with micrometer scanning resolution.

The aim of the present article is to review the recent progress in scanning SAXS/WAXS on hierarchical biological materials, with particular emphasis on the imaging potential of the method. It starts with a discussion of the current experimental possibilities, including some brief considerations about sample preparation and radiation damage in biological tissues. Then, recent work with scanning SAXS on bone and other mineralized tissues as well as scanning WAXS on wood and insect cuticle are reviewed, with special focus on the construction and interpretation of images obtained by mapping nanostructural information. We further discuss the determination of the local morphological and crystallographic orientation (texture) of crystalline fibers and particles. The combination of full three-dimensional (3D) texture analysis with x-ray microbeam scanning is presented for the examples of trabecular and osteonal bone. Finally, an outlook about some likely future directions and possibilities is given.

II. EXPERIMENTAL CONSIDERATIONS

All scanning techniques use the same fundamental principle, that is, to scan a sample across a fine probe, and to measure a signal arising from the interaction between the probe and the specimen. The interaction volume is given by the lateral size of the probe and its penetration depth into the specimen, defining the "position resolution" of the respective technique. Hence, the result of a scanning experiment is typically a two dimensional (2D) image showing the measured signal as a function of two scanning coordinates. One peculiarity of employing scanning x-ray microbeam scattering in connection with an area detector is that each scanning step does not only deliver a scalar signal value (as in scanning electron microscopy or scanning force microscopy) or a one-dimensional (1D) spectrum (as in many scanning spectroscopy methods), but a 2D scattering pattern. Establishing the method as a real imaging technique implies therefore the reduction and evaluation of these 2D scattering patterns to obtain images of nanostructural parameters as a direct output of the experiment. This step is not at all trivial, and considerable effort is currently undertaken by several groups and initiatives to reach this goal. Progress was recently achieved, in particular, in the fully automated tracking of peak positions[31–33] or the online or quasionline imaging of simple integral SAXS parameters such as the total scattered intensity or the mean chord length.[34]
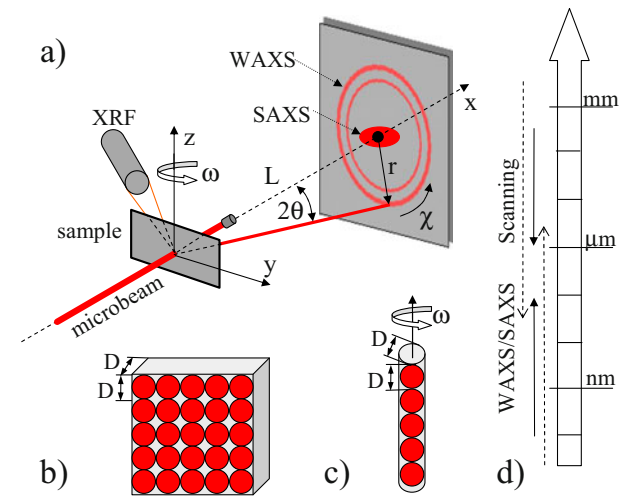
FIG. 1. (a) Scheme of a simultaneous microbeam SAXS/WAXS/XRF experiment. A microbeam impinges the thin sample in x direction. The SAXS/WAXS area detector is placed in the y-z plane at a distance L behind the specimen. The scattered intensity in polar detector coordinates $I(r,\chi)$ is converted into reciprocal space units $I(q,\chi)$, where the length of the scattering vector q is given by $q=4\pi \sin \theta/\lambda$, with $2\theta=\arctan(r/L)$ being the scattering angle and λ the x-ray wavelength. The XRF detector is positioned in the x-y plane, optimally almost perpendicular to the primary beam direction. The specimen can be scanned laterally within the y-z plane perpendicular to the primary beam and rotated around the z axis (rotation angle ω). (b) shows the optimum sample geometry and sample thickness D for 2D scanning and (c) shows the same for 1D scanning with sample rotation. Red circles symbolize the beam footprint. (d) shows the length scales (logarithmic scale) that can be simultaneously covered by the method, in principle (dashed lines), and in a current realistic experiment (full lines).

A. Experimental setup

The experimental setup for a typical scanning microbeam scattering experiment is quite simple and is sketched in Fig. 1(a). A thin sample is hit by an x-ray microbeam in transmission geometry and the scattered photons are collected with a high resolution area detector placed perpendicular to the primary x-ray beam. In addition to the position sensitive detector for x-ray scattering, an energy sensitive detector may additionally be employed to collect the x-ray fluorescence (XRF) radiation for chemical analysis. The sample is usually mounted on a high resolution goniometer with at least two translation axes and one rotation axis perpendicular to the beam. 2D scanning is typically performed in steps of about the beam diameter within a sheetlike sample with a thickness similar to the beam size [see Fig. 1(b)]. In this way, 2D scattering patterns as well as XRF spectra can be collected from sample volumes in the order of D^3 (D is the beam size) for each scanning step. While in a typical laboratory setup, D cannot be made much smaller than about 100 μm for primary intensity reasons,[9] synchrotron radiation allows readily to obtain beam sizes down to 10 μm at bending magnet and wiggler sources[30,35,36] and down to 1 μm at undulator sources at dedicated high energy x-ray facilities such as the ESRF.[11,13] Even though much smaller beam sizes have recently been demonstrated with hard x rays,[37–39] scattering experiments with beam sizes well below 1 μm are still far from being routine. The reasons for this are related to several

factors, including sample preparation and handling, sample visualization, and (long-time) beam stability issues. Nonetheless, current developments of long nanofocus beamlines promise stable experiment setups with routine beam sizes in the order of a few hundred nanometers within the next few years.

B. Simultaneous microbeam SAXS/WAXS

Due to the high brilliance of third generation synchrotron radiation sources, a large number of photons can be brought to the sample with a small beam size and a small beam divergence. This allows optimizing the experimental setup for a small beam at the sample position (determining the real space resolution for scanning) and at the detector position (determining the scattering or reciprocal space resolution) at the same time. When using additionally a large area detector with small pixel size, the detector can be placed very close to the sample (typically <200 mm). This allows constructing a very compact instrument covering SAXS and WAXS simultaneously.[30,40] A state of the art area detector (charge coupled device or pixel detector) with a point spread function <100 μm and edge length >200 mm allows to cover up to three orders of magnitude in the length of the scattering vector q simultaneously[30] (see Fig. 1 for the definition of q). Figure 2 shows an example of a SAXS/WAXS pattern from human trabecular bone with $q_{max}/q_{min}=250$. This large q range provides simultaneously crystallographic parameters from the carbonated hydroxyapatite (HAP) nanoparticles such as crystallographic texture or lattice parameter from WAXS, as well as the size shape and orientation of the HAP particles from SAXS (see Sec. II C).

From an instrumentation point of view, the biggest challenge is the reduction in parasitic background scattering to resolve weak SAXS signals and diffuse WAXS scattering. Air scattering is a serious issue, given that the total number of primary scattering particles (electrons) in an ≈ 200 mm long air path exceeds the one from a ≈ 0.1 mm thick (primarily organic) sample by typically a factor of 10–20. The same is of course true for any kind of x-ray windows used for sample containers. Putting the whole instrument into vacuum (or at least in a helium atmosphere) would be a solution to this dilemma. However, this option is seldom employed due to the loss of flexibility on the one hand, and due to the frequent need to keep biological tissues in a humid environment—and thus requiring windows—on the other hand. The specimen must be placed very close (typically less than 1 mm) to the final guard pinhole in order to entirely avoid air scattering from behind the sample. Otherwise, air scattering produces a shadow image of the sample and the sample holder on the area detector, which is very difficult to deal with. In order to minimize the (less critical) air scattering in front of the sample, a beam stop with a small diameter should be placed as close as possible to the sample. For the example shown in Fig. 2, a cylindrical beam stop (lead wire) of 0.25 mm diameter was placed at a distance of 50 mm from the sample. This relatively large distance leads to a considerable air scattering background at intermediate angles, indi-
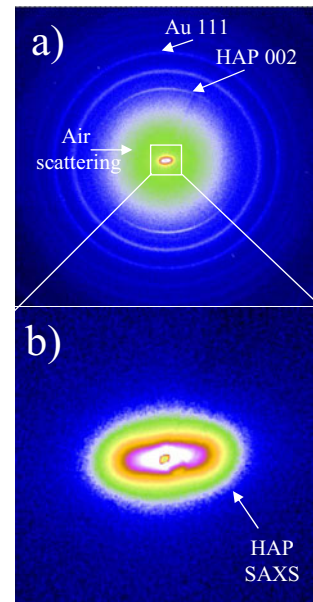

FIG. 2. Simultaneous SAXS/WAXS (raw data, no background subtracted) from a 20 μm thick section of human trabecular bone, measured at the μ-Spot beamline at the BESSY II synchrotron radiation source in Berlin, Germany. The pattern was collected with a MarMosaic-225 detector (MarUSA, Evanston, USA) using a 10 μm monochromatic beam from a W/Si multilayer (wavelength $\lambda=0.0827$ nm) at a sample detector distance $L=220$ mm. The covered range of scattering angles is $0.15°<2\theta<36°$, corresponding to 0.2 nm$^{-1}<q<47$ nm^{-1}. (a) shows the whole scattering pattern with the 002 reflection from the calcium phosphate mineral particles (carbonated HAP) and the 111 reflection from an internal gold standard indicated. (b) displays the enlarged region close to the direct beam, showing an anisotropic SAXS signal from nonspherical HAP nanoparticles. The intensity is visualized in a logarithmic color coded scale, blue corresponding to low and white to high intensity values.

cated by the isotropic halo in Fig. 2(a). Since the handling and stability of a much smaller beam stop is not easily possible, a reduction in air scattering can only be achieved on the cost of resolution toward small angles, as q_{min} is directly determined by the angular size of the beam stop. This means that one has usually to find a compromise between SAXS resolution and air scattering reduction.

These considerations illustrate that miniaturization (small beam stop and detector pixels, small distances) together with high beam brilliance (small beam size and divergence) is the way to choose for scanning SAXS/WAXS with high resolution in both real and reciprocal spaces. This fact is noteworthy insofar, as the usual way to increase resolution in scattering experiments was previously rather to build large instruments. It can be anticipated that a future dedicated scanning SAXS/WAXS instrument with, say, 100 nm beam size must be built even much more compact than current instruments.

C. Sample preparation

Sample preparation for scanning SAXS/WAXS experiments is a serious issue for hierarchical biological tissues, the efforts becoming comparable to sample preparation for TEM. The ideal sample for 2D scanning is a sheet with a

thickness comparable to the beam size in order not to loose the position resolution by averaging along the beam path [Fig. 1(b)]. If the specimen is additionally rotated during the experiment, the position resolution gets blurred in the direction perpendicular to the rotation axis and the specimen must be either even thinner, or must exhibit a local lamellar symmetry (see, e.g., Sec. IV). The ideal sample geometry for rotation (texture) experiments is thus a rod, with 1D scanning possibility along the rod axis [Fig. 1(c)]. The usual scanning experiment is conducted with a freestanding specimen, typically mounted (glued) on the tip of a tapered glass capillary. The use of micromanipulators can be very helpful in this respect, and becomes mandatory for very tiny samples of only a few micrometer size.[41]

Bone and other mineralized tissues are usually fixed and embedded into resin. Cutting with a diamond saw followed by grinding and polishing permits obtaining slices of a few micrometer thickness. Other tissues may require to be cut in their native (in particular, hydrated) state with a (cryo-) microtome, or with an UV microlaser. The latter, installed on an optical microscope, has proven to be a very useful and flexible tool in preparing thin slices of organic tissues, as there is no heat impact and the possibility to keep the sample in an aqueous environment.[33,41,42] Even though also focused ion beam techniques have obtained quite some attention in recent years, they are rarely used for the preparation of biological tissues.[43] This is mainly because of the need of ultrahigh vacuum conditions, and the possible "poisoning" of a surface layer by the Ga ions. It has generally to be mentioned that with all preparation techniques great attention must of course be paid on surface damage, which in the cases of micrometer sample thickness may be dominating over the undisturbed bulk volume.

D. Radiation damage

Radiation damage is not only one of the limiting steps in protein structure analysis via protein crystallography (see, e.g., Ref. 12) but also starts to play a considerable role in SAXS/WAXS investigations of biological tissues. There are only few papers and practically no systematic investigations of radiation damage in hierarchical biological tissues during scattering experiments with high brilliance synchrotron radiation, and its influence on the structural parameters extracted from SAXS/WAXS patterns is not well known. The crystal structure of organic crystalline phases such as cellulose or chitin is very sensitive to radiation damage by electrons or x-rays,[44,45] and a decay of the intensity of Bragg reflections with irradiation time is usually observed. To the personal experience of the author,[46] nanocrystalline cellulose fibrils in plants or chitin fibrils in arthropod cuticle show deterioration of crystallinity already after 1 min of exposure in air environment by a high brilliance undulator beam at the ESRF. It was also observed that the small-angle Bragg reflections arising from the axial d period of collagen broaden and shift within a period of minutes when illuminated with a flux $>10^{13}$ photons s^{-1} mm^{-2}.
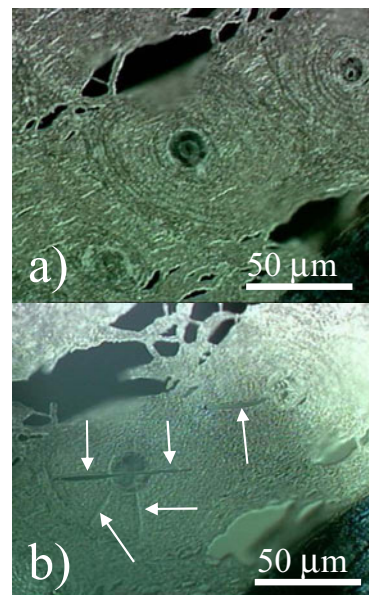

FIG. 3. Light microscopy images of a 5 μm thick section of demineralized human bone embedded in polymethylmethacrylate (PMMA). (a) After several hours of SAXS/WAXS measurements in a cryostream at a temperature of 100 K. (b) the same sample after reheating to room temperature ($\approx$300 K). Cracks (indicated by arrows) develop at the positions where previous SAXS/WAXS line scans were conducted at low temperature. Measurements were performed at the ESRF, beamline ID13 with a 0.3 μm beam at an x-ray energy E=13 keV (λ=0.095 nm).

It is well known that secondary damage due to free radical diffusion is one of the major sources of radiation damage in biological macromolecules.[47] One possibility to avoid secondary damage is to use radical scavengers, and/or to cool the specimen to cryogenic temperatures, avoiding the diffusion of free radicals. Figure 3 demonstrates that radiation damage can indeed be successfully "frozen in" within biological tissue, allowing to conduct scanning SAXS/WAXS experiments on highly radiation sensitive soft biological tissues. However, cryocooling creates constraints for the specimen environment and a considerable increase in background scattering, in particular, at small angles. Cryocooling is of course also not an option for *in situ* experiments, e.g., *in situ* deformation of biological tissues.[48,49] Other possibilities to cope with radiation damage are very fast measurements, which have become feasible with new developments of pixel detectors[50] in combination with scanning.[11,13] Due to the diffusion of radicals (the mean diffusion distance in water is in the order of several μm/s at room temperature[51]), there are also limits to this. Staying ahead of radiation damage requires therefore essentially much faster scanning as compared to now, which is, in principle, feasible with increased flux density and faster detectors. Finally, it should also be mentioned that the use of very small samples could, under certain conditions, result in a reduction in secondary radiation damage. Hence, the use of very small samples as originally proposed for protein crystallography[52] might well be a loophole to avoid or reduce radiation damage in biopolymers and biological tissues.

III. TOWARD SAXS IMAGING OF HIERARCHICAL BIOLOGICAL TISSUES

Bone is characterized by a rich structural hierarchy from macroscopic dimensions down to the molecular scale.[1–3] The basic building block of bone is the mineralized collagen fibril, consisting of staggered collagen type I triple helices with embedded platelike mineral particles of calcium phosphate [carbonated hydroxyapatite (HAP)]. Small-angle x-ray scattering has long been employed to study the size shape and arrangement of these mineral particles in human bone,[53,54] in particular, also in connection with bone diseases and treatment.[55,56] Two structural parameters are easily obtained from SAXS on bone using a pinhole camera with 2D detector [see, e.g., Fig. 2(b)]: (i) from the azimuthally averaged SAXS intensity $I(q)$, the mean chord length (or T parameter) is obtained, which is directly related to the average thickness of the plate-shaped mineral particles,[53,57] and (ii) the elliptical shape of the SAXS isointensity contour [Fig. 2(b)] gives information on the mean orientation and degree of orientation of the mineral platelets.[58] More detailed analysis permits obtaining additional information on the orientation distribution,[56] and the shape and arrangement of the particles.[59,60]

A. Imaging of bone nanostructure

Trabecular bone was probably the first biological tissue where the idea of scanning SAXS was successfully applied.[9,58] Employing a beam of 200 μm size from a laboratory SAXS instrument, nanostructural parameters such as the mineral particle thickness T, the mean particle orientation, and their degree of orientation could be mapped over extended areas with a resolution on the level of single trabeculae. This local information provides a new quality of understanding the relationship between the hierarchical structure of bone and its mechanical properties, in particular, in combination with other position sensitive methods such as quantitative electron backscattering,[61] energy dispersive x-ray analysis, and atomic force microscopy,[62] or Fourier-transformed infrared spectroscopy.[63] First scanning SAXS investigations on bone using synchrotron radiation were performed at the SAXS beamline at ELETTRA (Trieste, Italy) using a 20 μm wide x-ray beam.[10,35] These investigations were later extended to bone-cartilage interfaces,[10,64] and to mineralized avian tendons.[65]

To illustrate the important step from a microbeam SAXS experiment to SAXS imaging, we discuss a recent example of SAXS from osteons in more detail. The secondary osteon—a fundamental building block in compact bone—is a multilayered cylindrical structure of mineralized collagen fibrils arranged around a blood vessel, with one lamella being about 5–10 μm thick [see Fig. 4(a)]. It was already revealed with scanning SAXS using a 20 μm beam that there is a concentric arrangement of the mineral particles around the central hole in osteons.[10] To obtain information about the structural organization within the single lamellae in the osteon, SAXS patterns were collected at the ID13 beamline (ESRF, Grenoble) in a 2D mesh scan with 1 μm beam
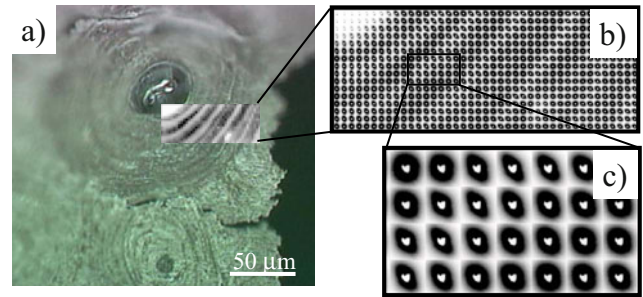

FIG. 4. SAXS imaging of a single osteon. (a) displays the light microscopy image of a 3 μm thick cortical bone section showing two osteons. The inset in (a) displays the image of the SAXS intensity in the selected region, obtained by binning the total SAXS intensity to a single pixel giving a gray value for each scanning step. The contrast mechanism leading to the observed SAXS intensity image is revealed by inspecting the single SAXS patterns (b) and (c). Within one lamella, the shape of the SAXS patterns changes in radial direction of the osteon from circular to strongly elliptical and back to circular again. A simple qualitative explanation of this contrast is based on the fact that plate-shaped mineral particles correspond roughly to a intensity distribution resembling a prolate ellipsoid in reciprocal space, the long axis corresponding to the direction of the plate normal. Since the measured SAXS pattern is simply a plane section through this ellipsoid, it is clear that the contrast is mainly determined by the local orientation of the mineral particles.

size employing the same step size.[34] The simplest image that can be derived online or quasionline during the scan is by binning all pixels of the SAXS signal on the area detector (or a selected region of interest) into one value. This image is shown in the inset in Fig. 4(a), displaying clearly the lamellar structure of the osteon. To understand the origin of the contrast, it is, in principle, necessary to analyze each single SAXS pattern quantitatively. It is, however, clear from the visual inspection of the 2D SAXS patterns [Figs. 4(b) and 4(c)] that the origin of the contrast is the ellipticity of the SAXS signal, which can be related to the mean local orientation of the mineral particles. Figure 4 therefore suggests that the mineral particle orientation changes continuously within one single lamella. To obtain the orientation quantitatively, the reconstruction of the full 3D SAXS "ellipsoid" in reciprocal space is necessary, which would necessitate additionally sample rotation. This point will be discussed in more detail in Sec. III B for WAXS on osteons.

Images from further nanostructural features can be obtained by evaluating the SAXS data quantitatively. In Fig. 5(a), the T parameter is shown for an osteon, while Fig. 5(b) shows the total SAXS intensity already discussed above, and Fig. 5(c) shows the x-ray transmission. The average mineral particle thickness T appears more or less constant (3.5–4.0 nm) across the osteon with a clear drop ($\approx$3 nm) at the innermost lamella. This indicates the well known fact that the younger bone in this region has smaller mineral particles.[61] It is also remarkable that the images of the T parameter and sample transmission do not (or only very weakly) show the lamellar structure, supporting the above interpretation of the orientation contrast observed in the total intensity image [Fig. 5(b)].
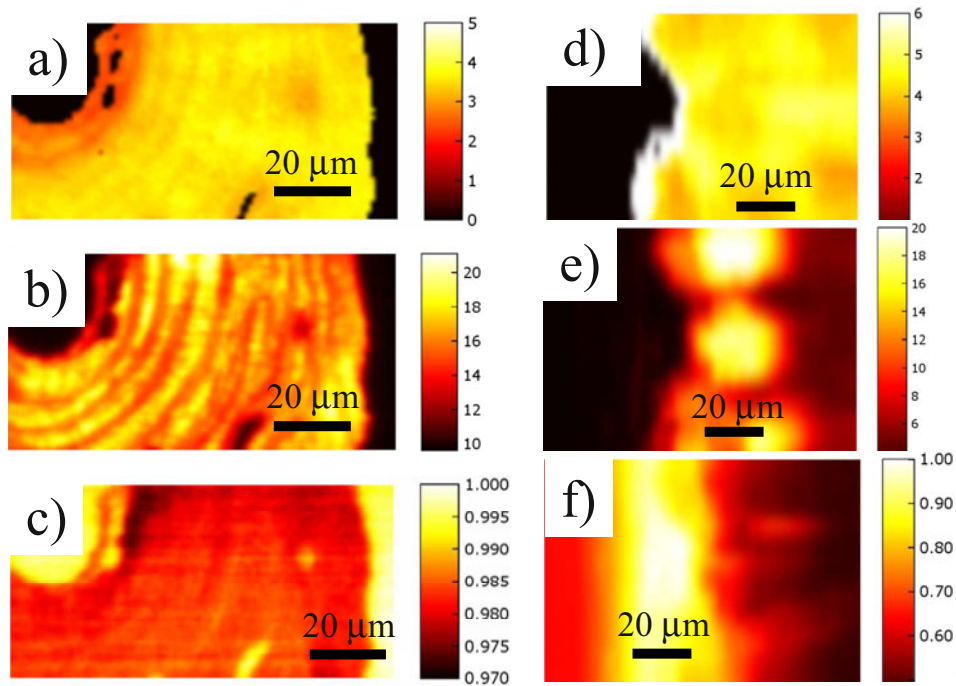
FIG. 5. Scanning SAXS images obtained from osteonal bone (a) to (c), and from hen eggshell (d) to (f). The images (a) and (d) show the mean chord length (T parameter), and (b) and (e) show the integrated SAXS intensity. Images (c) and (f) show the x-ray transmission through the sample, which is mainly determined by the local mineral density in these highly mineralized tissues. Figure reproduced from Gourrier *et al.*(Ref. 34) with permission from the International Union of Crystallography (http://journals.iucr.org).

B. Further examples of SAXS imaging

Another example of SAXS imaging is presented in Figs. 5(d)–5(f), obtained from a thin cross section of hen eggshell.[34] Starting from the inner membrane [bright stripe in Fig. 5(f)], the first mineralized layer is the mammillary layer, known to contain randomly oriented calcite crystals associated with an organic protein matrix.[66] The calcite crystals are in the order of 1 μm in size, and therefore, the SAXS signal must be attributed to inter- or intracrystalline matter, such as protein inclusions,[67] for instance. The T parameter is about 5 nm, and does not change much within the investigated region. Interestingly, again the total SAXS intensity shows a rich contrast [Fig. 5(e)], displaying spherulitic structures that are observable also in light microscopy images.[34] These structures are not associated with different mineral densities as proven by the x-ray transmission image in Fig. 5(f). Since the SAXS patterns were only slightly anisotropic, the change in intensity by more than a factor of 5 in the intensity image can also not be explained by an orientation contrast such as for the osteon. The most likely explanation is that the contrast is due to a local difference in protein content, since for low contents of organic material (<5%) the SAXS contrast would change roughly linear with the protein concentration.

Several groups have recently started to use 2D scanning SAXS for the mapping of quantitative nanostructural parameters of mineralized tissues, for instance, in archeological bone,[68] in newly formed bone adjacent to implants,[69] or in engineered bone at the bone scaffold interface.[70] Spatially resolved SAXS investigations in connection with position resolved measurements of chemical composition and mechanical properties using nanoindentation have also been employed for the investigation of dentin-enamel interfaces in teeth,[71] or biominerals in the jaws of marine worms.[72,73] Moreover, several studies dealing with the cross sectional structure of biopolymeric fibers were reported, for instance, on native cellulose fibers,[74] wool,[75] or human hair.[76]

IV. MAPPING CRYSTALLOGRAPHIC AND MOLECULAR ORIENTATION BY SCANNING WAXS

The intensity, position, and width of Bragg reflections from crystalline organic or inorganic components in biological materials contain useful information about local crystallographic and nanostructural features. Examples are the determination of crystallographic phases and their degree of crystallinity, as well as size and strains of nanocrystals. Moreover, crystalline entities in biological tissues are seldom randomly oriented (polycrystals), nor are they perfectly single crystalline. Using scanning WAXS, the orientation (and orientation distribution) of crystalline or semicrystalline entities in tissues can be obtained and mapped as a function of position by employing quantitative texture analysis. In general, the determination of the crystallographic orientation distribution requires rotation of the sample and the construction of so-called pole figures from intensities of several reflections measured on the unit sphere.[77,78]

As compared to single crystals, many fibrous crystalline biopolymers in natural tissues exhibit a local fiber texture. This means that a crystallographic fiber axis—corresponding to the morphological fiber direction—shows rotational sym-

metry around this axis. This leads to so called fiber diffraction patterns if the fiber axis is perpendicular to the primary x-ray beam. It can be generally shown[25,79] that the 3D orientation of the fiber axis can be determined from a single 2D diffraction pattern even if the fiber axis is not perpendicular to the x-ray beam. The reason is that the Ewald sphere curvature induces a symmetry breaking with respect to nonmeridional reflections if the fiber axis is tilted with respect to the primary beam.[79] Thus, scanning a thin sample with local fiber symmetry across a microbeam permits the imaging of the (3D) fiber orientation without sample rotation. It has to be noted that this fundamental principle is only applicable for x-ray diffraction where the wavelength λ is typically in the same order of magnitude as the sample lattice spacing. For electron diffraction or high energy x-rays the Ewald sphere can be considered to be flat for the relevant lattice spacings, hence necessitating sample rotation.

One application example is the determination of the cellulose fibril orientation in plants. The so-called microfibril angle, i.e., the spiral angle of cellulose fibrils with respect to the cell axis has been determined in a position resolved way already in 1994 by Jakob et al.[80] across the annual rings of spruce wood. These investigations were later extended to stems of different wood types,[81] and wood branches,[82] and related to the mechanical adaptation of wood to external loads.[83] The imaging of the local microfibril angle across single wood cells[25] can be seen as one of the pioneering experiments for scanning WAXS on complex biological tissues. Employing nonstandard diffraction geometry (x-ray beam direction parallel to the cell direction) together with a microbeam considerably smaller than the cell wall thickness, the spiraling cellulose orientation within adjacent cell walls was imaged for the first time within an intact tissue.[25]

In the following we present and discuss two more recent examples of WAXS imaging: the mapping of the local fiber orientation in complex shaped arthropod cuticle and the local morphological and crystallographic texture of mineral particles in bone.

A. Local fiber orientation in arthropod cuticle

Arthropods, the largest phylum of animals include among others the insects, spiders, and crustaceans. They are characterized by a hard exoskeleton or cuticle which is a hierarchical nanocomposite of stiff crystalline chitin fibers in a protein matrix, sometimes—in particular, in crustaceans—additionally reinforced with biominerals (mostly calcium carbonate). The arthropod cuticle is the prototype of a rotated or twisted plywood structure,[84,85] which is formed by the helicoidal stacking sequence of fibrous chitin-protein layers in the plane of the cuticle. Besides the cuticle, a multitude of jointed appendages basically also formed by chitin/protein nanocomposites are used for feeding, locomotion, and sensory reception. Particularly complex systems are, for instance, airflow sensors in spiders and insects.[86] Figures 6(a) and 6(b) shows the flow sensing systems in the appendices of a cricket. Each individual sensor comprises a stiff hair acting as a lever arm during airflow. As the tip of the hair moves to
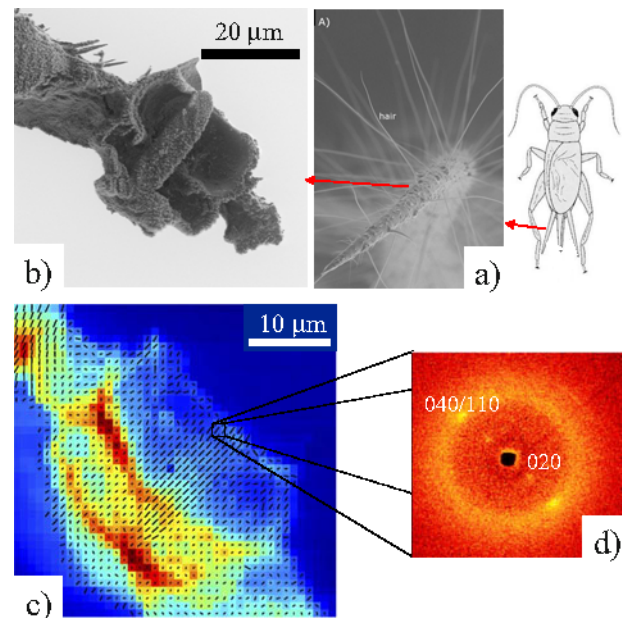

FIG. 6. WAXS imaging of the local chitin orientation in the flow sensing system of crickets. (a) shows a SEM image of the cricket appendix with the sensory hairs and (b) shows a SEM image of a single sensory system prepared by cutting with an UV microlaser. The whole socket including the hair (cut at the top of the socket) and its anchoring base are clearly visible. (c) displays the scanning WAXS image of the system in (b) with the color being the total azimuthally integrated intensity of the 040/110 doublet [see (d)]. The black lines in each pixel of the image visualize the local mean orientation of the chitin fiber axis (direction of the bar) and its degree of orientation (length of the bar). Figure in part reproduced from Seidel et al. (Ref. 33) with permission from Elsevier.

one side, the anchored base moves in the opposite direction, triggering a signal in the attached neuron. The hair sits in a complex socket [Fig. 6(b)] with two or more strain sensors (campaniforms) attached at the base of the socket. These strain sensors are believed to perceive additional information on the flow by detecting surface strains caused by the hair if it impacts on the rim of the socket.[86,87] In order to model the details of the stress distribution and amplification that leads to signal creation in the strain sensor,[88] the local orientation of the stiff chitin fibers in the whole flow sensing system is of paramount importance.

Figure 6(c) depicts a scanning WAXS image of the specimen shown in Fig. 6(b), obtained with a 0.3 μm x-ray beam at the microfocus beamline at the ESRF.[33] The color displays the total intensity of the chitin 040/110 reflection doublet. As the socket is a complex 3D object, the x-ray beam hits sample regions of different thicknesses and the intensity is thus indicative of the local chitin content, leading to a perfect projection image of the sensory system. The local fiber orientation was evaluated from the equatorial 040/110 reflections [Fig. 6(d)], and an orientation vector was plotted in Fig. 6(c) as a bar for each pixel of the scan. The direction of the bar gives the fiber orientation projected to the detector plane while the length of the bar symbolizes the degree of orientation. It is seen that the chitin fibers in the hair are perfectly parallel to the hair axis and have the highest orientation degree. For most of the other regions in the sensory system the

local orientation is rather difficult to interpret since the signal is being averaged over a long beam path within a complex shaped object. The only regions where reliable orientation information can be obtained apart of the hair are the walls of the socket. The fiber orientation here seems to be parallel to the hair, resembling essentially the orientation of the staves in a barrel. Since the socket transmits a mechanical signal to the campaniforms at its base, this fiber orientation makes sense in terms of a mechanical optimization.[33]

This example demonstrates that scanning WAXS without the necessity of sample rotation is able to image local fiber orientation in complex shaped functional units in hierarchical biological tissues, as long as local fiber symmetry can be assumed. However, it also clearly shows the restrictions which are particularly caused by such complex geometries, requiring, in principle, 3D (volume) sensitivity of the technique.

B. Quantitative texture analysis in bone

It is well known that the apatite c axis in bone is parallel to the collagen fiber axis.[89,90] Thus, determination of the HAP c-axis orientation can be used to determine the collagen orientation in bone. Since we cannot generally assume local fiber symmetry at a certain hierarchical level, a full 3D pole figure analysis of the 002 reflection is, in principle, necessary. Texture analysis in bone has already been employed since many years with x rays,[91–94] and neutrons,[95] but only little position resolved work on intact tissues has been reported so far. A comparison of the local crystallographic orientation of the mineral c axis with the morphological orientation of the mineral particles was recently undertaken in human trabecular bone.[96] This was achieved by constructing pole figures from 3D SAXS and WAXS data at the level of single trabeculae. This work revealed a close relationship between the c-axis orientation (crystallographic texture) and the mineral platelets (morphological texture), the plate normal being consistently perpendicular to the c axis (Fig. 7). Additionally, complementary information was deduced from the SAXS pole figures, revealing [Fig. 7(d)] that the mineral platelets are preferentially parallel to the lamellae within the trabecula [$S1-S3$ plane in Fig. 7(a)].

The second example is related to the position resolved, quantitative determination of the c-axis orientation (and thus the collagen fiber orientation) within the lamellae of an osteon.[97,98] The changing SAXS intensity within the lamellae as discussed in Sec. III A revealed a changing orientation of the mineral platelet normal within one lamella. A quantitative picture of the c-axis orientation can be obtained by performing a full 3D pole figure analysis of the 002 HAP reflection as a function of radial position across the osteon. Since the osteon exhibits a complex geometry, such experiments require a careful choice of the experimental geometry, together with very small dimensions of the x-ray beam and sample thickness [Fig. 8(a)]. The experiment revealed essentially that the c axis (and thus the collagen fiber direction) forms a helicoidal stack within each lamella with the helicoid rotation axis being perpendicular to the osteon axis [Fig. 8(b)].
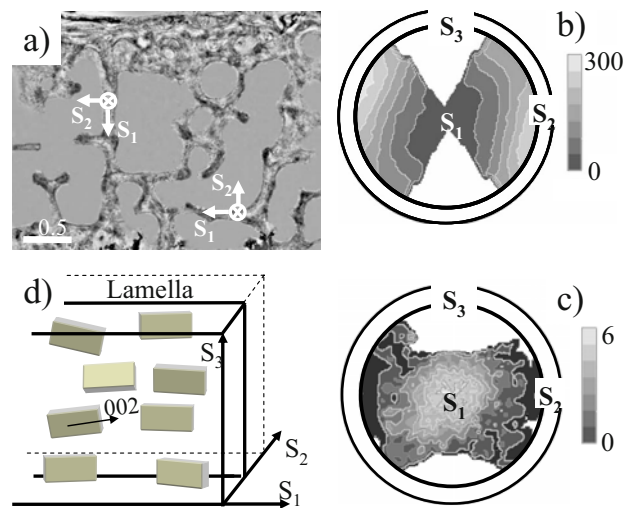

FIG. 7. Local SAXS/WAXS texture in trabecular human vertebral bone using a 200 μm x-ray beam from a laboratory source. (a) shows a light microscopy image from a 200 μm thick bone section embedded in PMMA, indicating also the local coordinate system (S_1, S_2, S_3) connected with the single trabeculae. Local pole figures were constructed from the 3D angular intensity distributions of the SAXS signal (b) and the 002 reflection from the hexagonal HAP nanocrystals (c). The WAXS pole figure provides the main orientation of the HAP c axis (highest pole density) in S_1 direction, whereas the SAXS pole figure suggests that the plate normal of the plate-shaped HAP nanoparticles points preferentially into a direction close to S_2. These findings are sketched in (d) for a single lamella within the trabeculae. Figure reproduced from Jaschouz *et al.* (Ref. 96) with permission from the International Union of Crystallography (http://journals.iucr.org).

This is a similar building principle as in the case of arthropod cuticle (see Sec. IV A), with the difference that the rotation in arthropod cuticle runs over 180°, forming an isotropic structure in the plane perpendicular to helicoid rotation axis. In the osteon, there is a preferred fiber orientation with respect to the osteon axis (about 30°), with the fiber axis being restricted within one quadrant. Together with the cylindrical shape of the osteon, this defines a spiraling arrangement of the fibrils with respect to the fiber axis [Fig. 8(c)]. The similarity to the orientation of cellulose microfibrils in wood cell walls[25] is amazing, and is an impressive example for a general building principle using helicoidal structures in nature.[84,85]

V. FUTURE DIRECTIONS

Even though imaging is not always the primary objective of scanning SAXS/WAXS yet, it is clear that the method has a great potential to evolve toward a real imaging technique. Our current work in progress focuses on the combination of simultaneous SAXS, WAXS, and XRF mapping, including online or quasionline extraction of several parameters for imaging. For bone, SAXS delivers the thickness as well as the orientation and orientation degree of the mineral platelets, and the evaluation of the Scherrer size[99] of the 002 reflection allows to estimate the long dimension of the mineral particles. Accurate determination of the lattice parameter [e.g., by using internal standards, see Fig. 2(a)] can reveal strains and/or variations of mineral composition, comple-
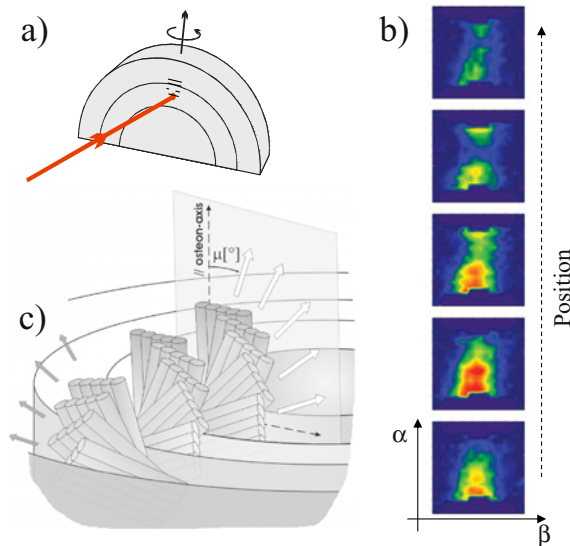
FIG. 8. Scanning texture analysis in human osteons using a 1 μm x-ray beam at the microfocus beamline ID13 (ESRF, Grenoble). (a) shows the geometry used for the measurements. A thin section containing a single osteon [compare Fig. 3(a)] was mounted with the osteon axis parallel to the primary beam and rotated from −45° to 45° in 5° steps around an axis perpendicular to the x-ray beam. 1D scanning was performed over the whole osteon parallel to the rotation axis. Since for a 3 μm thick sample and a 1 μm wide x-ray beam the lamellae can be considered flat in this geometry, sample rotation does not lead to a reduction in position resolution. (b) displays regrouped pole figures (radial pole angle α and azimuthal pole angle β, see original publications for definition) of the 002 reflection from five adjacent positions (1 μm step) within a single lamella. The maximum intensity (red color, corresponding to the main c-axis orientation) shifts continuously along the angular direction α, while it stays constant with respect to the angle β. This corresponds to a rotation of the c axis within the (local) plane of the lamellae. Since rotation of the sample at a fixed position provides exactly the same c-axis shift (see original publications), this gives the picture of a helicoidal orientation change of the c axis (and thus the collagen orientation) within each lamella, i.e., the helicoid rotation axis is perpendicular to the osteon axis (c). (b) was reproduced from Wagermaier et al. (Ref. 98) with permission from the International Union of Crystallography (http://journals.iucr.org), and (c) was reproduced from Wagermaier et al. (Ref. 97) with permission from the American Vacuum Society.

mented by the mapping of chemical composition by scanning XRF. In this way, several images with different information contents from exactly the same specimen areas are obtained. In bone research, this approach may lead in the long term to the development of dedicated and highly specialized instruments for medical screening applications in bone and other connective tissues. Synchrotron radiation sources permit micrometer and submicrometer image resolution, while future laboratory instruments based on x-ray microsources may allow position resolution down to at least 50 μm.

A generally very promising future direction is the combination of different position resolved techniques. Simultaneous SAXS/WAXS and XRF have already been mentioned above, and also the application of online (polarized) light microscopy is possible without great difficulty. A remarkable recent development with a large potential for biological tissues is the combination of SAXS/WAXS with simultaneous Raman spectroscopy.[100,101] Future instrumentation with

nanobeams will particularly also require new ways of sample visualization, since optical light microscopy is not applicable anymore below 1 μm. First ideas exist to implement AFM and near field optics into nanofocus beamlines.

A further important future direction will be the combination of position resolved SAXS/WAXS with in situ experiments. Mechanical deformation combined with mapping of the local nanostructural changes has already been demonstrated in other fields, e.g., for in situ bending of carbon fibers[102] or crack propagation in polymers.[103] Such techniques will be of great value to get deeper insight in the relationship between local structure and mechanical properties, for instance, concerning the fracture toughness of bone.[104] Furthermore, humidity control combined with in situ position resolved SAXS/WAXS may be used to further investigate such fascinating phenomena as the recently reported humidity induced actuation in plant tissues.[105] Another fascinating development—although not directly related to hierarchical tissues—is the application of optical tweezers to catch and manipulate very small particles (e.g., single vesicles, cells) in solution in combination with microbeam SAXS/WAXS.[106]

One of the advantages of x rays over many other techniques is their large penetration depth into matter, and therefore the principle possibility to obtain 3D information from bulk specimens in a nondestructive way. 3D absorption-, phase- and spectroscopic imagings are nowadays almost routinely offered at synchrotron radiation sources using different techniques such as computed tomography or confocal scanning. These developments are not yet very advanced for x-ray scattering techniques with 3D position resolution in biological tissues. Confocal x-ray diffraction, for instance, is based on the 3D scanning of a subvolume within the sample defined by the intersection of primary and diffracted beam. While this technique has been quite successfully applied to metals,[107,108] the extension to biological materials is not trivial due to their much more complex structure, and no serious attempts have been reported so far. Another technique—energy variable diffraction—uses the energy dependence of the x-ray penetration depth,[109] and has been applied to study the in-depth microstructure in mollusk shells.[110] Together with 2D scanning using a microbeam, this technique would, in principle, also be able to give 3D diffraction information. A very interesting recent approach is SAXS tomography,[111] which is based on "first generation tomography," i.e., a combination of sample scanning and sample rotation and using standard reconstruction algorithms. The authors have shown that the SAXS signal parallel to the rotation axis can be reconstructed uniquely with full 3D position resolution given essentially by the beam size. Unfortunately, the restriction to random orientation or fiber symmetry of the scattering particles limits this technique to rather simple cases which are usually not given in hierarchical biological tissues. A similar approach has recently also been reported for WAXS on a bone specimen using selected HAP reflections,[112] although no comprehen-

sive theoretical treatment was yet undertaken to clarify the limitations of this approach for textured materials.

Finally, an entirely new class of imaging techniques based on x-ray scattering with potential 3D resolution should also be mentioned here. These techniques are frequently summarized under the label "coherent x-ray diffraction imaging" (CXDI), and are based on the reconstruction of real space images from SAXS speckle patterns obtained using coherent or partly coherent x rays.[113] More general, the fundamental principle of the CXDI technique is based on the numerical Fourier transform of the far-field coherent x-ray diffraction pattern. It has been shown, for instance, that the 3D imaging of strains in submicron particles is possible,[114] and a recent paper has reported first CXDI measurements on bone.[115] Current limitations are, in particular, restrictions concerning the rather small sample sizes required (typically a few hundred nanometers), which might, however, in practice, be less serious as recent CXDI results on cells have demonstrated.[116] Current developments permit that these methods will complement or even replace the scanning SAXS/WAXS techniques for the investigation of the hierarchical structure of biological materials. First attempts have already been made to combine CXDI with scanning using strongly focused beams in the submicrometer range.[117,118]

ACKNOWLEDGMENTS

[1] S. Weiner and H. D. Wagner, Annu. Rev. Mater. Sci. **28**, 271 (1998).

[2] P. Fratzl, H. S. Gupta, E. P. Paschalis, and P. Roschger, J. Mater. Chem. **14**, 2115 (2004).

[3] P. Fratzl and R. Weinkamer, Prog. Mater. Sci. **52**, 1263 (2007).

[4] D. Fengel and G. Wegener, *Wood: Chemistry, Ultrastructure, Reactions*, (de Gruyter, Berlin, 1989).

[5] P. Fratzl, I. Burgert, and H. S. Gupta, Phys. Chem. Chem. Phys. **6**, 5575 (2004).

[6] A. C. Neville, *Biology of the Arthropod Cuticle* (Springer, Berlin, 1975).

[7] J. Vincent and U. Wegst, Arthropod Struct. Dev. **33**, 187 (2004).

[8] R. Roer and R. Dillaman, Am. Zool. **24**, 893 (1984).

[9] P. Fratzl, H. F. Jakob, S. Rinnerthaler, P. Roschger, and K. Klaushofer, J. Appl. Crystallogr. **30**, 765 (1997).

[10] O. Paris, I. Zizak, H. Lichtenegger, P. Roschger, K. Klaushofer, and P. Fratzl, Cell. Mol. Biol. Lett. **46**, 993 (2000).

[11] C. Riekel, Rep. Prog. Phys. **63**, 233 (2000).

[12] C. Riekel, M. Burghammer, and G. Schertler, Curr. Opin. Struct. Biol. **15**, 556 (2005).

[13] C. Riekel and R. J. Davies, Curr. Opin. Colloid Interface Sci. **9**, 396 (2005).

[14] C. Riekel, A. Cedola, F. Heidelbach, and K. Wegner, Macromolecules **30**, 1033 (1997).

[15] C. Riekel, T. Dieing, P. Engstrom, L. Vincze, C. Martin, and A. Mahendrasingam, Macromolecules **32**, 7859 (1999).

[16] C. Riekel, M. Muller, and F. Vollrath, Macromolecules **32**, 4464 (1999).

[17] C. Riekel, M. C. G. Gutierrez, A. Gourrier, and S. Roth, Anal. Bioanal. Chem. **376**, 594 (2003).

[18] M. Grosse, J. Boehmer, and C. Riekel, J. Mater. Sci. Lett. **17**, 1631 (1998).

[19] D. Loidl, H. Peterlik, O. Paris, M. Müller, M. Burghammer, and C. Riekel, J. Synchrotron Radiat. **12**, 758 (2005).

[20] A. Mahendrasingam et al., J. Synchrotron Radiat. **2**, 308 (1995).

[21] M. Muller, C. Riekel, R. Vuong, and H. Chanzy, Polymer **41**, 2627 (2000).

[22] R. J. Davies, M. A. Montes-Moran, C. Riekel, and R. J. Young, J. Mater. Sci. **36**, 3079 (2001).

[23] A. Bram, C. I. Branden, C. Craig, I. Snigireva, and C. Riekel, J. Appl. Crystallogr. **30**, 390 (1997).

[24] T. A. Waigh, I. Hopkinson, A. M. Donald, M. F. Butler, F. Heidelbach, and C. Riekel, Macromolecules **30**, 3813 (1997).

[25] H. Lichtenegger, M. Muller, O. Paris, C. Riekel, and P. Fratzl, J. Appl. Crystallogr. **32**, 1127 (1999).

[26] F. Baltenneck, B. A. Bernard, J. C. Garson, P. Engstrom, C. Riekel, F. Leroy, A. Franbourg, and J. Doucet, Cell. Mol. Biol. Lett. **46**, 1017 (2000).

[27] A. Bigi, M. Burghammer, R. Falconi, M. H. J. Koch, S. Panzavolta, and C. Riekel, J. Struct. Biol. **136**, 137 (2001).

[28] J. Schoeck, R. J. Davies, A. Martel, and C. Riekel, Biomacromolecules **8**, 602 (2007).

[29] M. Peura, M. Muller, U. Vainio, M. P. Saren, P. Saranpaa, and R. Serimaa, Trees-Structure and Function **22**, 49 (2008).

[30] O. Paris, C. Li, S. Siegel, G. Weseloh, F. Emmerling, H. Riesemeier, A. Erko, and P. Fratzl, J. Appl. Crystallogr. **40**, s466 (2007).

[31] R. J. Davies, J. Appl. Crystallogr. **39**, 262 (2006).

[32] R. J. Davies, J. Appl. Crystallogr. **39**, 267 (2006).

[33] R. Seidel, A. Gourrier, M. Burghammer, C. Riekel, G. Jeronimidis, and O. Paris, Micron **39**, 198 (2008).

[34] A. Gourrier et al., J. Appl. Crystallogr. **40**, s78 (2007); http://journals.iucr.org/

[35] I. Zizak, O. Paris, P. Roschger, S. Bernstorff, H. Amenitsch, K. Klaushofer, and P. Fratzl, J. Appl. Crystallogr. **33**, 820 (2000).

[36] Y. Nozue, R. Kurita, S. Hirano, N. Kawasaki, S. Ueno, A. Iida, T. Nishi, and Y. Amemiya, Polymer **44**, 6397 (2003).

[37] F. Pfeiffer, C. David, M. Burghammer, C. Riekel, and T. Salditt, Science **297**, 230 (2002).

[38] O. Hignette, P. Cloetens, W. K. Lee, W. Ludwig, and G. Rostaing, J. Phys. IV **104**, 231 (2003).

[39] C. G. Schroer et al., Appl. Phys. Lett. **87**, 164102 (2005).

[40] C. Riekel, M. Burghammer, and M. Muller, J. Appl. Crystallogr. **33**, 421 (2000).

[41] R. J. Davies, C. Koenig, M. Burghammer, and C. Riekel, Appl. Phys. Lett. **92**, 101903 (2008).

[42] M. Ruggeberg, T. Speck, O. Paris, C. Lapierre, G. Koch, and I. Burgert, Proc. R. Soc. London, Ser. B (to be published).

[43] S. Orso, U. G. K. Wegst, C. Eberl, and E. Arzt, Adv. Mater. (Weinheim, Ger.) **18**, 874 (2006).

[44] E. Takacs, L. Wojnarovits, J. Borsa, C. Foldvary, P. Hargittai, and O. Zold, Radiat. Phys. Chem. **55**, 663 (1999).

[45] A. Gemperle, Z. Holan, and V. Pokorny, Biopolymers **21**, 1 (1982).

[46] O. Paris (unpublished).

[47] R. Henderson, Proc. R. Soc. London, Ser. B **241**, 6 (1990).

[48] H. Gupta, J. Seto, W. Wagermaier, P. Zaslansky, P. Boesecke, and P. Fratzl, Proc. Natl. Acad. Sci. U.S.A. **103**, 17741 (2006).

[49] R. Puxkandl, I. Zizak, O. Paris, J. Keckes, W. Tesch, S. Bernstorff, P. Purslow, and P. Fratzl, Philos. Trans. R. Soc. London, Ser. B **357**, 191 (2002).

[50] C. Broennimann et al., J. Synchrotron Radiat. **13**, 120 (2006).

[51] C. R. Wilke and P. Chang, AIChE J. **1**, 264 (1955).

[52] C. Nave and M. A. Hill, J. Synchrotron Radiat. **12**, 299 (2005).

[53] P. Fratzl, N. Fratzl-Zelman, K. Klaushofer, G. Vogl, and K. Koller, Calcif. Tissue Int. **48**, 407 (1991).

[54] P. Fratzl, M. Groschner, G. Vogl, H. Plenk, J. Eschberger, N. Fratzlzelman, K. Koller, and K. Klaushofer, J. Bone Miner. Res. **7**, 329 (1992).

[55] P. Fratzl, P. Roschger, J. Eschberger, B. Abendroth, and K. Klaushofer, J. Bone Miner. Res. **9**, 1541 (1994).

[56] P. Fratzl, O. Paris, K. Klaushofer, and W. J. Landis, J. Clin. Invest. **97**, 396 (1996).

[57]P. Fratzl, S. Schreiber, and K. Klaushofer, Connect. Tissue Res. **35**, 9 (1996).

[58]S. Rinnerthaler, P. Roschger, H. F. Jakob, A. Nader, K. Klaushofer, and P. Fratzl, Calcif. Tissue Int. **64**, 422 (1999).

[59]P. Fratzl, H. S. Gupta, O. Paris, A. Valenta, P. Roschger, and K. Klaushofer, Prog. Colloid Polym. Sci. **130**, 33 (2005).

[60]P. Fratzl, J. Stat. Phys. **77**, 125 (1994).

[61]P. Roschger, B. M. Grabner, S. Rinnerthaler, W. Tesch, M. Kneissel, A. Berzlanovich, K. Klaushofer, and P. Fratzl, J. Struct. Biol. **136**, 126 (2001).

[62]M. Hauge Bunger *et al.*, Bone (N.Y.) **39**, 530 (2006).

[63]N. P. Camacho, S. Rinnerthaler, E. P. Paschalis, R. Mendelsohn, A. L. Boskey, and P. Fratzl, Bone (N.Y.) **25**, 287 (1999).

[64]I. Zizak *et al.*, J. Struct. Biol. **141**, 208 (2003).

[65]H. S. Gupta, P. Roschger, I. Zizak, N. Fratzl-Zelman, A. Nader, K. Klaushofer, and P. Fratzl, Calcif. Tissue Int. **72**, 567 (2003).

[66]D. Lammie, M. M. Bain, and T. J. Wess, J. Synchrotron Radiat. **12**, 721 (2005).

[67]E. Zolotoyabko and B. Pokroy, Cryst. Eng. Commun. **9**, 1156 (2007).

[68]J. C. Hiller and T. J. Wess, J. Archaeol. Sci. **33**, 560 (2006).

[69]M. H. Bunger *et al.*, Eur. Cells Mater **12**, 81 (2006).

[70]A. Cedola *et al.*, Spectrochim. Acta, Part B **62**, 642 (2007).

[71]W. Tesch, N. Eidelman, P. Roschger, F. Goldenberg, K. Klaushofer, and P. Fratzl, Calcif. Tissue Int. **69**, 147 (2001).

[72]H. C. Lichtenegger, T. Schoberl, M. H. Bartl, H. Waite, and G. D. Stucky, Science **298**, 389 (2002).

[73]H. C. Lichtenegger, T. Schoberl, J. T. Ruokolainen, J. O. Cross, S. M. Heald, H. Birkedal, J. H. Waite, and G. D. Stucky, Proc. Natl. Acad. Sci. U.S.A. **100**, 9144 (2003).

[74]M. Muller, C. Czihak, G. Vogl, P. Fratzl, H. Schober, and C. Riekel, Macromolecules **31**, 3953 (1998).

[75]Y. Kajiura, S. Watanabe, T. Itou, A. Iida, Y. Shinohara, and Y. Amemiya, J. Appl. Crystallogr. **38**, 420 (2005).

[76]Y. Kajiura *et al.*, J. Struct. Biol. **155**, 438 (2006).

[77]H. Bunge, *Texture Analysis in Materials Science* (Butterworths, London, 1982).

[78]H. R. Wenk and P. Van Houtte, Rep. Prog. Phys. **67**, 1367 (2004).

[79]O. Paris and M. Muller, Nucl. Instrum. Methods Phys. Res. B **200**, 390 (2003).

[80]H. F. Jakob, P. Fratzl, and S. E. Tschegg, J. Struct. Biol. **113**, 13 (1994).

[81]H. Lichtenegger, A. Reiterer, S. E. Stanzl-Tschegg, and P. Fratzl, J. Struct. Biol. **128**, 257 (1999).

[82]J. Farber, H. C. Lichtenegger, A. Reiterer, S. Stanzl-Tschegg, and P. Fratzl, J. Mater. Sci. **36**, 5087 (2001).

[83]A. Reiterer, H. Lichtenegger, S. Tschegg, and P. Fratzl, Philos. Mag. A **79**, 2173 (1999).

[84]A. C. Neville, *Biology of Fibrous Composites: Development Beyond the Cell Membrane* (Cambridge University Press, Cambridge, 1993).

[85]M. M. Giraud-Guille, Curr. Opin. Solid State Mater. Sci. **3**, 221 (1998).

[86]T. A. Keil, Microsc. Res. Tech. **39**, 506 (1997).

[87]J. S. Edwards and J. Palka, Proc. R. Soc. London, Ser. B **185**, 83 (1974).

[88]A. Skordos, P. H. Chan, J. F. V. Vincent, and G. Jeronimidis, Philos. Trans. R. Soc. London, Ser. A **360**, 239 (2002).

[89]S. Weiner, W. Traub, and H. D. Wagner, J. Struct. Biol. **126**, 241 (1999).

[90]W. J. Landis, K. J. Hodges, J. Arena, M. J. Song, and B. F. McEwen, Microsc. Res. Tech. **33**, 192 (1996).

[91]F. Heidelbach, C. Riekel, and H. R. Wenk, J. Appl. Crystallogr. **32**, 841 (1999).

[92]H. R. Wenk and F. Heidelbach, Bone (N.Y.) **24**, 361 (1999).

[93]A. Ascenzi, A. Benvenuti, A. Bigi, E. Foresti, M. H. J. Koch, F. Mango, A. Ripamonti, and N. Roveri, Calcif. Tissue Int. **62**, 266 (1998).

[94]N. Sasaki and Y. Sudoh, Calcif. Tissue Int. **60**, 361 (1997).

[95]G. E. Bacon, P. J. Bacon, and R. K. Griffiths, J. Appl. Crystallogr. **10**, 124 (1977).

[96]D. Jaschouz, O. Paris, P. Roschger, H. S. Hwang, and P. Fratzl, J. Appl. Crystallogr. **36**, 494 (2003); http://journals.iucr.org/

[97]W. Wagermaier, H. S. Gupta, A. Gourrier, M. Burghammer, P. Roschger, and P. Fratzl, BioInterphases **1**, 1 (2006).

[98]W. Wagermaier, H. S. Gupta, A. Gourrier, O. Paris, P. Roschger, M. Burghammer, and R. C. P. Fratzl, J. Appl. Crystallogr. **40**, 115 (2007); http://journals.iucr.org/

[99]H. P. Klug and L. E. Alexander, *X-ray Diffraction Procedures* (Wiley, New York, 1974).

[100]R. J. Davies, M. Burghammer, and C. Riekel, Appl. Phys. Lett. **87**, 24105 (2005).

[101]R. J. Davies, M. Burghammer, and C. Riekel, Macromolecules **39**, 4834 (2006).

[102]D. Loidl, O. Paris, M. Burghammer, C. Riekel, and H. Peterlik, Phys. Rev. Lett. **95**, 225501 (2005).

[103]C. Lorenz-Haas, P. Muller-Buschbaum, O. Wunnicke, C. Cassignol, M. Burghammer, C. Riekel, and M. Stamm, Langmuir **19**, 3056 (2003).

[104]H. Peterlik, P. Roschger, K. Klaushofer, and P. Fratzl, Nat. Mater. **5**, 52 (2006).

[105]R. Elbaum, L. Zaltzman, I. Burgert, and P. Fratzl, Science **316**, 884 (2007).

[106]D. Cojoc *et al.*, Appl. Phys. Lett. **91**, 234107 (2007).

[107]H. F. Poulsen *et al.*, J. Appl. Crystallogr. **34**, 751 (2001).

[108]B. C. Larson, W. Yang, G. E. Ice, J. D. Budai, and J. Z. Tischler, Nature (London) **415**, 887 (2002).

[109]E. Zolotoyabko and J. P. Quintana, Rev. Sci. Instrum. **73**, 1663 (2002).

[110]B. Pokroy and E. Zolotoyabko, J. Mater. Chem. **13**, 682 (2003).

[111]C. G. Schroer, M. Kuhlmann, S. V. Roth, R. Gehrke, N. Stribeck, A. Almendarez-Camarillo, and B. Lengeler, Appl. Phys. Lett. **88**, 164102 (2006).

[112]S. R. Stock, F. de Carlo, and J. D. Almer, J. Struct. Biol. **161**, 144 (2008).

[113]J. W. Miao, P. Charalambous, J. Kirz, and D. Sayre, Nature (London) **400**, 342 (1999).

[114]M. A. Pfeifer, G. J. Williams, I. A. Vartanyants, R. Harder, and I. K. Robinson, Nature (London) **442**, 63 (2006).

[115]H. Jiang *et al.*, Phys. Rev. Lett. **100**, 038103 (2008).

[116]D. Shapiro *et al.*, Proc. Natl. Acad. Sci. U.S.A. **102**, 15343 (2005).

[117]H. M. L. Faulkner and J. M. Rodenburg, Phys. Rev. Lett. **93**, 023903 (2004).

[118]J. M. Rodenburg and H. M. L. Faulkner, Appl. Phys. Lett. **85**, 4795 (2004).